Paleocene latitude of the Kohistan–Ladakh arc indicates multistage India–Eurasia collision

Paleocene latitude of the Kohistan–Ladakh arc indicates multistage India–Eurasia collision

Craig R. Martin[a,1], Oliver Jagoutz[a], Rajeev Upadhyay[b], Leigh H. Royden[a], Michael P. Eddy[c], Elizabeth Bailey[d], Claire I. O. Nichols[a], and Benjamin P. Weiss[a]

[a]Department of Earth, Atmospheric and Planetary Sciences, Massachusetts Institute of Technology, Cambridge, MA 02139; [b]Department of Geology, Kumaun University, 263 002 Nainital, India; [c]Department of Earth, Atmospheric, and Planetary Sciences, Purdue University, West Lafayette, IN 47907; and [d]Department of Astronomy and Astrophysics, University of California, Santa Cruz, CA 95064

Edited by B. Clark Burchfiel, Massachusetts Institute of Technology, Cambridge, MA, and approved October 5, 2020 (received for review May 6, 2020)

We report paleomagnetic data showing that an intraoceanic Trans-Tethyan subduction zone existed south of the Eurasian continent and north of the Indian subcontinent until at least Paleocene time. This system was active between 66 and 62 Ma at a paleolatitude of 8.1 ± 5.6 °N, placing it 600–2,300 km south of the contemporaneous Eurasian margin. The first ophiolite obductions onto the northern Indian margin also occurred at this time, demonstrating that collision was a multistage process involving at least two subduction systems. Collisional events began with collision of India and the Trans-Tethyan subduction zone in Late Cretaceous to Early Paleocene time, followed by the collision of India (plus Trans-Tethyan ophiolites) with Eurasia in mid-Eocene time. These data constrain the total postcollisional convergence across the India–Eurasia convergent zone to 1,350–2,150 km and limit the north–south extent of northwestern Greater India to <900 km. These results have broad implications for how collisional processes may affect plate reconfigurations, global climate, and biodiversity.

India | paleomagnetism | Neotethys | Himalaya | intraoceanic arc

Classically, the India–Eurasia collision has been considered to be a single-stage event that occurred at 50–55 million years ago (Ma) (1, 2). However, plate reconstructions show thousands of kilometers of separation between India and Eurasia at the inferred time of collision (3, 4). Accordingly, the northern extent of Greater India was thought to have protruded up to 2,000 km relative to present-day India (5, 6) (Fig. 1). Others have suggested that the India–Eurasia collision was a multistage process that involved an east–west trending Trans-Tethyan subduction zone (TTSZ) situated south of the Eurasian margin (7–9) (Fig. 1). Jagoutz et al. (9) concluded that collision between India and the TTSZ occurred at 50–55 Ma, and the final continental collision occurred between the TTSZ and Eurasia at 40 Ma (9, 10). This model reconciles the amount of convergence between India and Eurasia with the observed shortening across the India–Eurasia collision system with the addition of the Kshiroda oceanic plate. Additionally, the presence of two subduction systems can explain the rapid India–Eurasia convergence rates (up to 16 mm a^{-1}) that existed between 135 and 50 Ma (9), as well as variations in global climate in the Cenozoic (11).

While the existence of the TTSZ in the Cretaceous is not disputed, the two conflicting collision models make distinct predictions about its paleolatitude in Late Cretaceous to Paleocene time; these can be tested using paleomagnetism. In the single-stage collision model, the TTSZ amalgamated with the Eurasian margin prior to ∼80 Ma (12) at a latitude of ≥20 °N (13, 14). In contrast, in the multistage model, the TTSZ remained near the equator at ≤10 °N, significantly south of Eurasia, until collision with India (9) (Fig. 1).

No undisputed paleomagnetic constraints on the location of the TTSZ are available in the central Himalaya (15–17). Westerweel et al. (18) showed that the Burma Terrane, in the eastern Himalaya, was part of the TTSZ and was located near the equator at ∼95 Ma, but they do not constrain the location of the TTSZ in the time period between 50 and 80 Ma, which is required to test the two collision hypotheses. In the western Himalaya, India and Eurasia are separated by the Bela, Khost, and Muslimbagh ophiolites and the 60,000 km^2 intraoceanic Kohistan Ladakh arc (19, 20) (Fig. 1). These were obducted onto India in the Late Cretaceous to Early Paleocene (19), prior to the closure of the Eocene to Oligocene Katawaz sedimentary basin (20) (Fig. 1). The Kohistan–Ladakh arc contacts the Eurasian Karakoram terrane in the north along the Shyok suture and the Indian plate in the south along the Indus suture (21) (Fig. 1). Previous paleomagnetic studies suggest that the Kohistan–Ladakh arc formed as part of the TTSZ near the equator in the early Cretaceous but provide no information on its location after 80 Ma (22–25). While pioneering, these studies lack robust age constraints, do not appropriately average paleosecular variation of the geodynamo, and do not demonstrate that the measured magnetizations have not been reset during a subsequent metamorphic episode.

Paleomagnetism of the Khardung Volcanics

Paleocene volcanic rocks from the Kohistan–Ladakh arc provide an unrivaled opportunity to use paleomagnetism to reconstruct the paleolatitude of the TTSZ shortly before onset of collision and test the two conflicting models. We sought to determine the paleolatitude of the Paleocene Khardung volcanics on the northern margin of the Kohistan–Ladakh arc in Ladakh, India. The ∼3,000-m-thick stratigraphy of the Khardung volcanics formed between 70 and 60 Ma (26, 27) and comprises rhyolitic and andesitic

Significance

We present paleomagnetic constraints on the latitude of an intraoceanic subduction system that is now sutured between India and Eurasia in the western Himalaya. Our results demonstrate that the India–Eurasia collision was a multistage process involving at least two subduction systems rather than a single-stage event. This resolves the discrepancy between the amount of convergence and the observed crustal shortening in the India–Eurasia collision system, as well as the 10–15 Ma time lag between collision onset in India and the initiation of collision-related deformation and metamorphism in Eurasia. The presence of an additional subduction system in the Neotethys ocean explains the rapid India–Eurasia convergence rates in the Cretaceous and global climate variations in the Cenozoic.

Author contributions: O.J., L.H.R., and B.P.W. designed research; C.R.M., O.J., R.U., L.H.R., and B.P.W. performed research; C.R.M., M.P.E., E.B., C.I.O.N., and B.P.W. analyzed data; and C.R.M., O.J., R.U., L.H.R., M.P.E., E.B., C.I.O.N., and B.P.W. wrote the paper.

The authors declare no competing interest.

This article is a PNAS Direct Submission.

[1]To whom correspondence may be addressed. Email: crm7@mit.edu.

This article contains supporting information online at https://www.pnas.org/lookup/suppl/doi:10.1073/pnas.2009039117/-/DCSupplemental.

First published November 4, 2020.

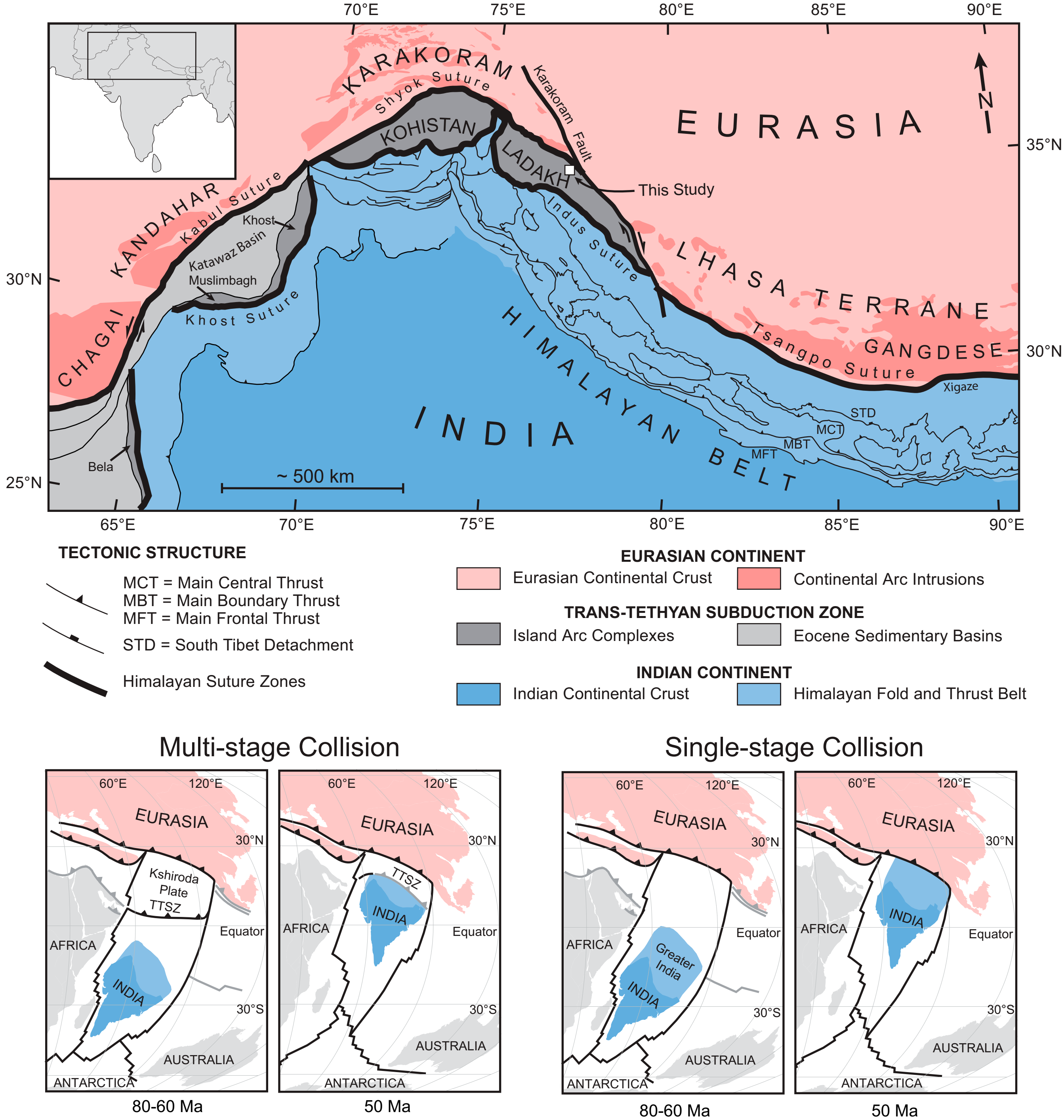

Fig. 1. The first panel is an overview map of tectonic structure of the Karakoram–Himalaya–Tibet orogenic system. Blue represents India, red represents Eurasia, and the Kohistan–Ladakh arc (KLA) is shown in gray. The different shades of blue highlight the deformed margin of the Indian plate that has been uplifted to form the Himalayan belt, and the zones of darker red within the Eurasian plate highlight the Eurasian continental arc batholith. Thick black lines denote the suture zones which separate Indian and Eurasian terranes. The tectonic summary panels illustrate the two conflicting collision models and their differing predictions of the location of the Kohistan–Ladakh arc. India is shown in blue, Eurasia is shown in red, and the other nearby continents are shown in gray. Active plate boundaries are shown with black lines, and recently extinct boundaries are shown with gray lines. Subduction zones are shown with triangular tick marks.

lava flows, tuffs, ignimbrites, agglomerate, and minor clastic sediments at the top of the section (*SI Appendix*, Figs. S1 and S2).

Zircons from ash layers and lava flows distributed throughout the upper 1,000 m of the exposed section were dated using U-Pb chemical abrasion–isotope dilution–thermal ionization mass spectrometry (CA-ID-TIMS) geochronology (*SI Appendix*, Table S1 and Fig. S4). The U-Pb ages are consistently younger from the bottom to the top of the stratigraphy indicating that there are no major repetitions or duplications caused by unidentified fault zones. Zircons separated from a rhyolite flow (LB13–17) sampled from the bottom part of the studied section yield a Th-corrected $^{206}Pb/^{238}U$ weighted mean eruption/deposition age of 65.038 ± 0.12

Ma (2σ external uncertainty), and zircons from the intermediate ash layer (KA1) yield a Th-corrected $^{206}Pb/^{238}U$ weighted mean eruption/deposition age of 62.097 ± 0.079 Ma. Two samples yielded inherited zircon populations, such that only a maximum depositional age could be constrained from the youngest zircon in the sample. The rhyolite flow sampled from the top of the section (LB13–16) has a Th-corrected $^{206}Pb/^{238}U$ zircon maximum depositional age of 61.636 ± 0.11 Ma, and the interlayered ash horizon (KA4D) at the bottom of the sampled stratigraphy has a Th-corrected $^{206}Pb/^{238}U$ zircon maximum depositional age of 66.100 ± 0.085 Ma. Based on these results the absolute time within our sampled section is 61.64–66.10 Ma, a time span of 4.46 Ma (Fig. 2).

We obtained a total of 191 oriented 2.2-cm-diameter cores from 21 sites across the dated section. At each site, the orientations of multiple bedding planes were measured, and a site-specific mean was calculated and applied to the magnetic data to correct for bedding tilt (Fig. 3). The sites used to estimate the paleolatitude each consist of 5–13 core samples from single flows that should have acquired a near-instantaneous (a few hours) thermoremanent magnetization from the local magnetic field as they cooled. For most samples, low-coercivity/low-temperature (LCT) overprints were removed using alternating field (AF) demagnetization steps between 1 and 20 mT and thermal demagnetization steps between 100 °C and 300 °C (*SI Appendix*, Figs. S7 and S8). Stable high-temperature magnetization components consistent with magnetite were isolated in the thermal demagnetization steps between 500 °C and 580 °C. In a small subset of the samples, stable, high-temperature components unblocking between 600 °C and 680 °C consistent with hematite were also present, oriented parallel to the magnetite component (*SI Appendix*, Fig. S7 and Dataset S1).

We confirmed the absence of significant posteruption remagnetization using a reversal test and two conglomerate tests consisting of 69 cores from clasts from two intraformational conglomerate units near the top and bottom of the sampled section (29) (*SI Appendix*, Figs. S9 and S10). The high-temperature magnetization directions from the clasts in the conglomerate units are random with ≥95% certainty (30), therefore indicating a lack of total remagnetization since deposition. The paleomagnetic measurements of the bedded volcanics define two antipodal populations (Fig. 3) extending over three geomagnetic polarity reversals that correlate to chrons C29n, C28r, C28n, C27r, and C26r, showing that they have not been overprinted (28) (Fig. 2). Our successful conglomerate tests and reversal test unequivocally demonstrate that the HT1 and HT2 directions in the samples are primary (29, 31).

We obtained a Fisher mean paleomagnetic pole located at a latitude of 64.0 °N and a longitude of 266.4 °E with a 95% confidence angle of $A_{95} = 5.6°$ (*SI Appendix*, Fig. S12). Secular variation should have been successfully averaged by our measurements given the >4-Ma time span recorded within the section (including three reversals) and the fact that the value of A_{95} is within the observed range for the modern geomagnetic field ($5.3° < A_{95} < 13.3°$, for $n = 18$) (29, 31, 32). The measured paleomagnetic pole constrains the paleolatitude of the Kohistan–Ladakh arc to 8.1 ± 5.6 °N at 61.64–66.10 Ma, significantly south of the Eurasian margin which was situated at 21.2 ± 2.1 °N at the same time (14). This constrains the location of the TTSZ to 600–2,300 km south of the Eurasian margin in the Paleocene (Fig. 4).

Discussion

Our results indicate that until at least ∼61.6 Ma, and probably until 50–55 Ma, the Neotethys ocean was subducted along two separate subduction systems, an active continental system at the southern Eurasian margin and the TTSZ located in the equatorial Neotethys (7–9) (Fig. 4). These findings support multistage tectonic evolution models for the western Himalaya in which the India–TTSZ–Eurasia collision began with collision between the TTSZ and the northern margin of India in the Late Cretaceous to Paleocene and ended with final continental collision in the mid-Eocene (9, 10) (Fig. 4).

The termination of intraoceanic subduction during the first stage of collision resulted in the Late Cretaceous/Early Paleocene obduction of the Bela, Muslimbagh, and Khost ophiolites onto the northwestern margin of India (19), as well as the formation of the 50–55 Ma Indus suture zone between the Kohistan–Ladakh arc and India (10). It also caused a reduction in the rate of northward motion of India at 52 ± 4 Ma (9). The final India–TTSZ–Eurasia continent–continent collision occurred along the Shyok–Tsangpo suture, not the Indus–Tsangpo, and the age of this final collision is constrained to 40.4 ± 1.3 Ma by geochemical and isotopic changes in the Kohistan–Ladakh batholith (10). This explains why the India–Eurasia convergence rate continued to decrease until 40–45 Ma (33).

Recent Cretaceous age estimates for the Kohistan–Ladakh arc–Eurasia collision based on sediment provenance interpretations of detrital zircon U-Pb age data (34, 35) are incompatible with our results. We note that Borneman et al. (35) report that Eurasia-derived detrital zircons were deposited on Kohistan–Ladakh arc rocks at 80 Ma despite previous work showing that the sediments they sampled were deposited on the Eurasian margin, not the Kohistan–Ladakh arc (36–38). Similarly, Najman et al. (34) interpret a uniquely Eurasian provenance for seven 200–220 Ma grains from Paleocene Indian passive margin sediments, but these could have been reworked from Late Triassic and Early Jurassic Indian passive margin sediments which contain similar age populations (39, 40). Unlike our paleomagnetic data, these detrital zircon provenance investigations are limited by the fact that the vast area of Greater Indian landmass, now lost beneath Tibet, likely contributed detritus of unknown age to passive margin sediments before the collision.

Geological evidence for a multistage collision history of the Himalaya is best preserved in the western Himalaya, where the Kohistan–Ladakh arc and other ophiolite bodies clearly demarcate the TTSZ, and east of the Namche Barwa syntaxis, where the TTSZ is represented by the Burma Terrane (18). The exposure of the Kohistan–Ladakh arc is ∼200 km wide in northeast Pakistan but reduces to <20 km in southwestern Tibet where it disappears at the intersection of the great counter thrust system and the Karakoram fault (41) (Fig. 1). In south central Tibet the record of the TTSZ is fragmentary due to the large-scale backthrusting along the great counter thrust system that obscures the complex evolution of the Tsangpo suture zone (42–44). It is not surprising that the geological record of the multiple stages of the India–TTSZ–Eurasia collision is limited in the central part of the Himalayan belt, where shortening and underthrusting were presumably highest.

The dismembered ophiolites in the Tsangpo suture zone could have formed in the TTSZ (7, 45), or in the forearc of the continental margin (17, 46). While the Xigaze ophiolite likely formed on the southern edge of Eurasia, it has recently been suggested that it moved southward in the Cretaceous during back arc extension after 85–90 Ma, becoming part of the TTSZ (44). However, subduction along the TTSZ initiated in the Jurassic [∼154 Ma (47)] and not in the Cretaceous. Alternatively, if the TTSZ and Xigaze units are unrelated, fragments of the TTSZ could remain unidentified in the accretionary mélange south of the Xigaze ophiolite or elsewhere in the less well studied areas of the suture zone. Regardless, our results require that a major oceanic basin existed in between India and Eurasia at the same time Cretaceous arc detritus was deposited in Indian passive margin sediments in southeastern Tibet at 58.5–60 Ma (48), making the TTSZ the likely sedimentary source rather than Eurasia.

The near-equatorial location of the TTSZ in the Paleocene implies that a significant proportion of the 2,800–3,600 km India–Eurasia convergence since 50–55 Ma (49) can be accounted

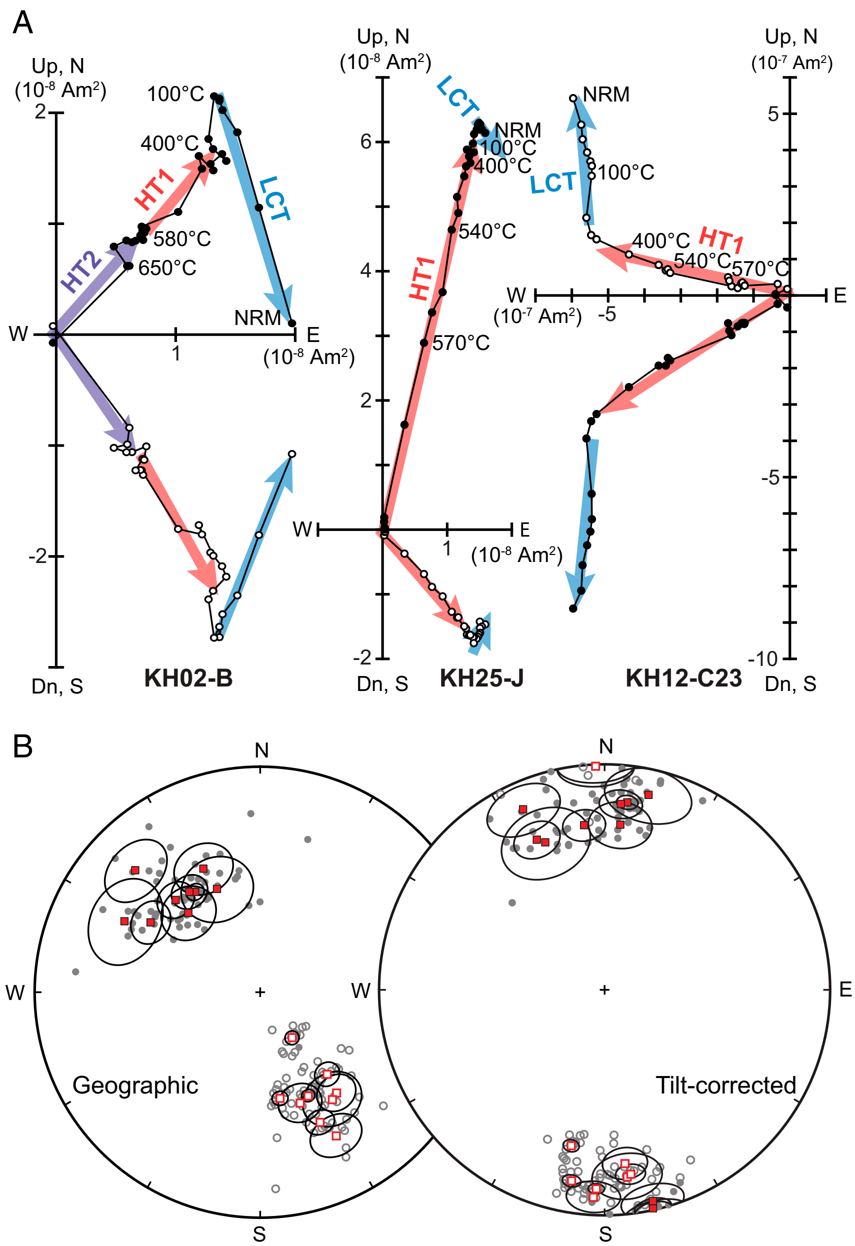

Fig. 2. (*A*) Orthographic projection diagrams showing AF and thermal demagnetization of three representative samples KH02-B, KH25-J, and conglomerate clast KH12–C23. Data are presented in geographic coordinates; closed symbols represent north–south–east–west projections, and open symbols represent up–down–east–west projections. Interpretations are shown with colored arrows: each arrow reflects a direction vector corresponding to components inferred from PCA. LCT = low-coercivity/low-temperature overprint, HT1 = high-temperature magnetite, HT2 = high-temperature hematite. (*B*) Stereographic equal-area projections showing HT1 directions for each sample (gray circles) and their site-means (red squares) with associated 95% confidence angles (black ellipses). Data are presented in geographic coordinates (*Left*) and after tilt correction (*Right*). Upward directions are denoted with open symbols, and downward directions are denoted with filled symbols.

for by precollisional subduction of the Kshiroda oceanic plate beneath Eurasia until ∼40 Ma rather than by thickening and extrusion of Indian and Eurasian continental crust. Indeed, the extrusion of southeast Asia started later, at ∼36 Ma (50), and metamorphism and melting in the High Himalaya began after 40 Ma (51). Comparison of our data to the well-constrained paleolatitudes of the Eurasian margin and India (13, 14) suggests that the Kshiroda plate was 1450 ± 850 km wide, at the time of the TTSZ–India collision (Fig. 4). Therefore, the convergence accommodated by deformation in the Himalayan orogen was 1,350–2,150 km, similar to the 1,050–1,950 km combined Eurasian and Indian shortening observed across western and eastern Tibet and the Himalayan fold and thrust belt (6, 52). Our results also constrain the size of Greater India in the western Himalaya to <900 km, consistent with the observed ∼600-km extent of Indian continental lithosphere underthrusted beneath Eurasia (53) and reconstructions of Greater India based on Cretaceous paleomagnetic data (14).

In conclusion, we present robust and reliable paleomagnetic data constraining the location of the TTSZ to 8.1 ± 5.6 °N in the Paleocene, 600–2,300 km south of the Eurasian margin. Our results require that two subduction zones were active throughout

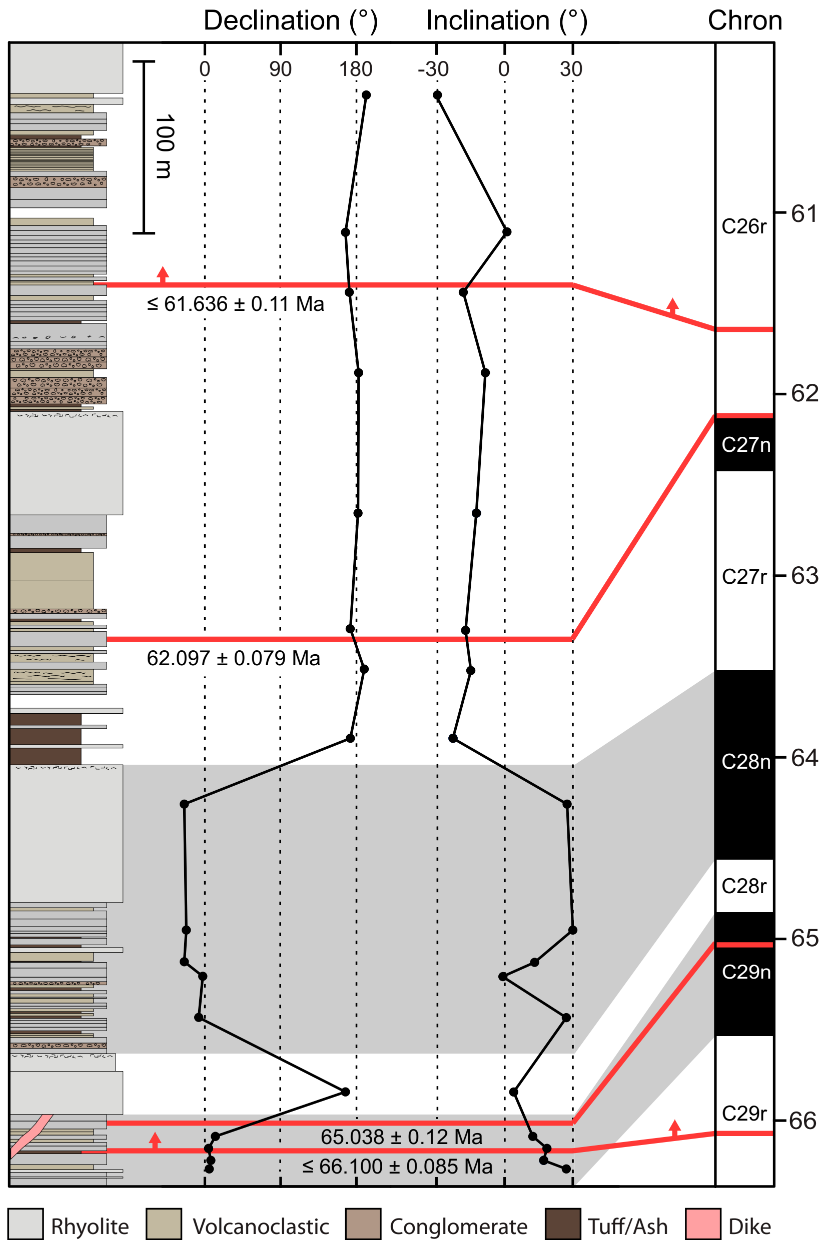

Fig. 3. Stratigraphic column of upper ∼1,000 m of Khardung volcanics where we collected paleomagnetic and geochronology samples. Rock types are denoted by the color of the blocks (gray = rhyolite, yellow = volcaniclastic, light brown = conglomerate, dark brown = tuff/ash, red = intermediate dike), the horizontal extent of the blocks represents the relative erosive prominence of the units in the field, and breaks in the section reflect small areas with no exposure. The site-mean declinations and inclinations are plotted against stratigraphic height, and our four U-Pb ages (2σ external uncertainty) are shown as red lines; up arrows indicate maximum depositional ages. The gray shaded regions show the correlation of the magnetic reversals in the sequence to the documented C29n, C28r, C28n, C27r, and C26r chrons which have been plotted with their age in the right-hand column (28).

the closure of the Neotethys until the Paleocene. We have also shown that the India–Eurasia collision was a multistage process that began with the accretion of the TTSZ onto India in the Late Cretaceous to Paleocene and ended with continent–continent collision in the Eocene at ∼40 Ma. The north–south extent of Greater India in the west was ∼900 km, and the final collision occurred along the Shyok–Tsangpo suture zone, not the Indus–Tsangpo. The combined activity of both Neotethyan subduction systems explains the anomalously rapid motion of India in the Late Cretaceous (9), and the low-latitude obduction of ophiolites associated with the two stages of India–Eurasia collision caused the global cooling observed throughout the Cenozoic (11). Our study demonstrates that the peripheries of the Himalayan belt provide crucial insight into the geological evolution of the India–TTSZ–Eurasia collision system that is difficult to discern in the central part of the orogen.

Materials and Methods

U-Pb Zircon Geochronology. Zircons were separated from each sample using standard crushing and density separation techniques. U-Pb geochronology was completed using the CA-ID-TIMS technique at Massachusetts Institute of Technology (MIT), following methods slightly modified from Mattinson (54) and outlined in the appendix to Eddy et al. (55). Zircons were first annealed at 900 °C and 1 atm for 60 h. Subsequently, individual zircons were loaded into Teflon microcapsules with 100–125 μL of 29M HF. The microcapsules were then loaded into a Parr dissolution vessel and held at 215 °C for 12–13 h.

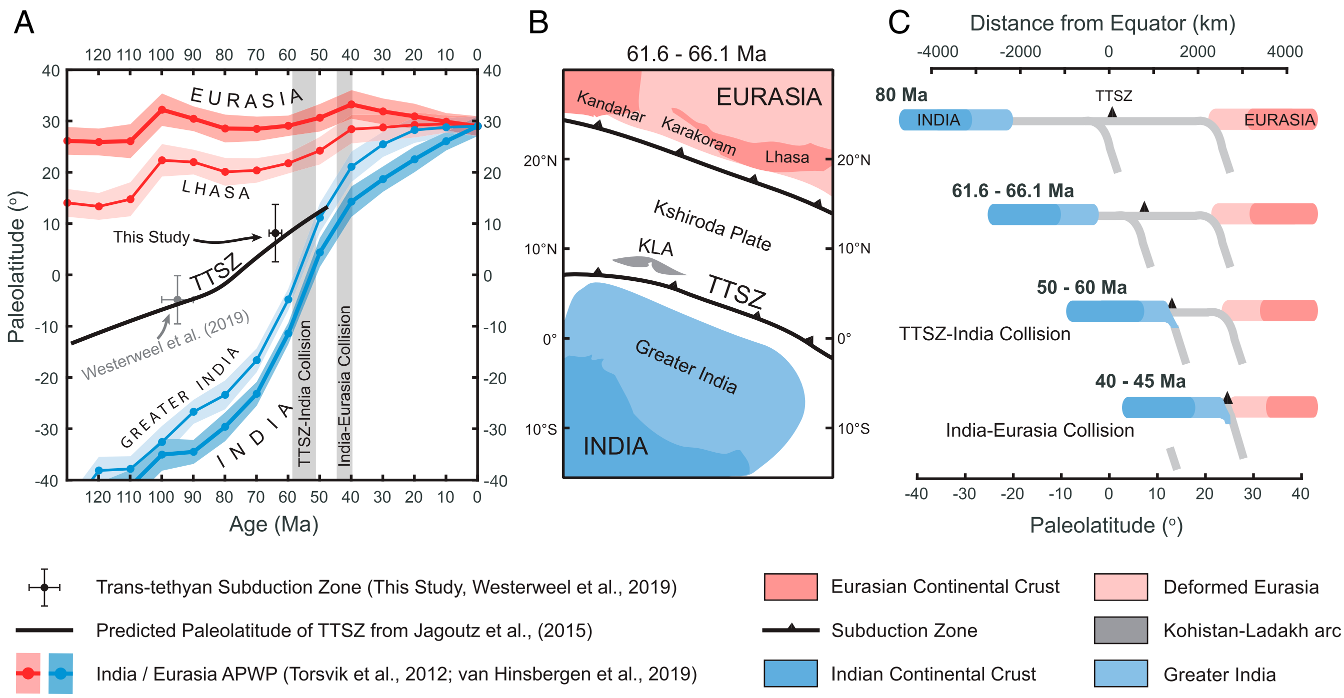

Fig. 4. (*A*) Paleolatitude of the TTSZ constrained at the KLA (this study) and the Burma Terrane (18) compared to paleomagnetic plate reconstructions of Indian and Eurasian terranes (4, 14) and the predicted location of the TTSZ (9) throughout the closure of the Neotethys ocean. (*B*) Paleogeographic map of the location of Kohistan–Ladakh arc relative to India and Eurasia in the Paleocene. The position of the Kohistan–Ladakh arc is reconstructed using our paleomagnetic pole from the Khardung volcanics, and the locations of Indian and Eurasian tectonic blocks are from the plate reconstruction of van Hinsbergen et al. (14). (*C*) Cross-section illustration showing the plate tectonic configuration of the India–TTSZ–Eurasia collision at 80 Ma, 61.6–66.1 Ma (constrained by our data), 50–60 Ma, and 40–45 Ma.

The resulting solutions were discarded, and each individual zircon was repeatedly rinsed in H_2O, and 6N HCl. After rinsing, approximately ∼0.01 g of EARTHTIME ^{202}Pb-^{205}Pb-^{233}U-^{235}U isotopic tracer (56) and 75–100 μL of 29M HF were added to each microcapsule. The microcapsules were then reloaded into a Parr dissolution vessel and held at 215 °C for 48–60 h for total digestion. The solutions were subsequently dried down and dissolved in 6N HCl at 180 °C for ∼12 h to convert the samples to chloride form. Uranium and Pb were purified from the dissolved sample with AG-1 X8 200–400 mesh anion exchange resin using methods modified from Krogh et al. (57). Samples were first loaded onto 50 μL anion exchange columns in 50–75 μL of 3N HCl and rinsed dropwise to remove trace elements. Then Pb and U were eluted using 200 μL of 6N HCl and 250 μL of H_2O, respectively. Samples were dried down with a microdrop of 0.05M H_3PO_4 prior to analysis via TIMS.

All of the data presented in this study were analyzed on the IsotopX Phoenix TIMS or the VG Sector 54 TIMS at MIT. Lead was run as a metal and measured by peak-hopping on a Daly photomultiplier. Uranium was analyzed as UO_2 and was measured statically on a series of Faraday cups. Measured ratios were corrected assuming an ^{18}O/^{16}O of 0.00205 ± 0.00004 (2 σ), corresponding to the modern atmospheric value of Nier (58). Corrections for mass-dependent fractionation of U were done using the known ratio of ^{233}U/^{235}U in the ET535 isotopic tracer and assuming a ^{238}U/^{235}U of 137.818 ± 0.045 (2 σ), which represents the mean value of ^{238}U/^{235}U measured in natural zircon (59). Corrections for Pb fractionation were done using an α (% amu) calculated from repeat runs of the NBS 981 Pb isotopic standard for the IsotopX Phoenix TIMS and an α calculated from 53 Pb measurements on the Sector 54 TIMS of the ET2535 isotopic tracer, which contains a known ^{202}Pb/^{205}Pb ratio.

A well-known problem in the measurement of small amounts of Pb by TIMS is the effect of isobaric interferences. Known isobaric interferences include $BaPO_4$ and Tl and were corrected by measuring masses 201 and 203, assuming that they represent $^{201}BaPO_4$ and ^{203}Tl, and using the natural abundances of $^{202}BaPO_4$, $^{204}BaPO_4$, $^{205}BaPO_4$, and ^{205}Tl to correct the measurements of masses 202, 204, and 205. These corrections were often minor and have no effect on our data interpretations.

A correction for common Pb (Pb_c) was done by assuming that all Pb_c is from laboratory contamination and using the measured ^{204}Pb and a laboratory Pb_c isotopic composition to subtract the appropriate mass of Pb_c from each analysis. We consider the assumption that all measured Pb_c is from laboratory contamination to be robust because the typical Pb_c seen in zircon analyses (<1 pg) is comparable to the mass of Pb_c seen in procedural blanks. One hundred forty-nine procedural blanks were used to quantify the Pb_c isotopic composition at MIT of ^{206}Pb/^{204}Pb = 18.13 ± 0.96 (2 σ), ^{207}Pb/^{204}Pb = 15.28 ± 0.60 (2 σ), ^{208}Pb/^{204}Pb = 37.04 ± 1.77 (2 σ).

A correction for initial secular disequilibrium in the ^{238}U-^{206}Pb system due to the exclusion of Th during zircon crystallization (e.g., 60) was made for each analysis using a ratio of zircon/melt partition coefficients (f_{ThU}) of 0.119. This value was determined from coexisting zircon rims/surfaces and high-SiO_2 glass from a dacitic lava from Mt. St. Helens (61). We view this as the best available analog for silicic, hydrous, arc magmatism. Nevertheless, we have applied a generous uncertainty of ±1 (2 σ) for the calculated [Th/U] magma.

All data reduction was done with the Tripoli and ET_Redux software packages (62) using the algorithms presented by McLean et al. (63). The U decay constants are from Jaffey et al. (64). All isotopic data are presented in *SI Appendix*, Table S1. Our age interpretations for each sample include weighted mean eruption/deposition ages for those samples that contain a coherent age population (LB13–17 and KA1) and maximum depositional ages for samples that did not include a coherent population (KA4D and LB13–16). These samples may have incorporated xenocrysts during eruption/deposition, and we conservatively use the youngest grain as a maximum age. All uncertainties within the text are reported as external 2 σ to aid in comparison with other geochronologic datasets produced by other techniques within the orogenic belt.

Paleomagnetism. Core samples were drilled in the field using a water-cooled electric hand drill. Cores were oriented in the field using an ASC Industries Pomeroy orienting fixture and extracted from the outcrop using nonmagnetic brass tools. One paleomagnetic specimen was cut from each core sample at MIT using an ASC Scientific dual-blade rock saw. Measurements of the natural remanent magnetization were obtained in the MIT Paleomagnetism Laboratory using a 2G Enterprises Superconducting Rock Magnetometer equipped with an automated sample handler (65) inside a mu-metal magnetically shielded room with <200-nT DC field. The specimens were subjected to stepwise AF and thermal demagnetization. AF steps were applied in increments of

4 mT up to 20 mT and followed by thermal steps starting at 100 °C and increasing up to 600 °C or 680 °C in variable interval sizes from a maximum of 100 °C and minimum of 5 °C close to the Curie temperatures of the suspected principal magnetic carriers, magnetite (580 °C) and hematite (680 °C). Stable components of magnetization were isolated using principal component analysis (PCA) (66) (see *SI Appendix*, Fig. S6 for examples of typical sample demagnetizations and Dataset S1 for all fitting data). The domain state of magnetite was assessed using hysteresis curves (*SI Appendix*, Figs. S4 and S5) that were measured for a representative subset of bedded volcanic samples (KH01B, KH03F, KH14A, and KH25A) on an ADE model 1660 vibrating sample magnetometer (VSM) in the Ross Laboratory, MIT Department of Materials Sciences and Engineering.

Site-mean magnetization directions were calculated using Fisher (67) statistics and corrected for bedding tilt (Fig. 2 and *SI Appendix*, Table S3). We calculated Northern Hemisphere virtual geomagnetic pole (VGP) positions for each site (*SI Appendix*, Table S3 and Fig. S11), then we took the Fisher (67) mean of the VGP data to obtain the overall paleomagnetic mean pole and associated A_{95} error envelope. We used the quantile–quantile method (68) to show that the VGP distribution is consistent with a Fisher model (*SI Appendix*, Fig. S10).

To test for postdepositional remagnetization, we performed two conglomerate tests and a reversal test (29). The conglomerate test samples consisted of cores from 46 clasts from an intraformational conglomerate unit at site KH12 (near the top of the section) and 23 clasts from another intraformational conglomerate unit at site KP3 (near the bottom of the section) (*SI Appendix*, Fig. S8). We performed a Watson (30) test for randomness on the distribution of tilt-corrected magnetic components from the clast specimens in each conglomerate unit. Both sets of conglomerate clast magnetization directions passed the conglomerate test, indicating that the clast magnetization directions were primary (see *SI Appendix* for further details). We used the bootstrap reversal test of Tauxe (69) to demonstrate that the two populations of site-mean magnetization directions from the volcanic sequence are antipodal to each other, therefore passing the reversal test (*SI Appendix*, Fig. S9). All paleomagnetic data reduction and interpretation were carried out using the PmagPy software package (70).

Data Availability. All study data are included in the article and supporting information.

Note Added in Proof. The description of the geochronology methods in this paper is similar to that in ref. 71.

ACKNOWLEDGMENTS. We thank Jade Fischer, Benjamin Klein, and Claire Bucholz for field assistance; C. P. Dorjay for logistical assistance; and Tsewang Dorjay, Stanzin Khando, and their family for accommodation at the Silok guesthouse in Khardung village, Ladakh. We also thank Athena Eyster, Caue Borlina, Jay Shah, and Eduardo Lima for assistance with paleomagnetic and rock magnetic experiments at the MIT Paleomagnetism Laboratory and MIT Ross Laboratory, and Neel Chatterjee for assistance in the MIT Electron Microprobe Facility. This work was funded by the NSF Tectonics Program and financially supported by the MIT International Science and Technology Initiatives India student travel program.

1. E. Garzanti, A. Baud, G. Mascle, Sedimentary record of the northward flight of India and its collision with Eurasia (Ladakh Himalaya, India). *Geodin. Acta* **1**, 297–312 (1987).
2. K. V. Hodges, Tectonics of the Himalaya and southern Tibet from two perspectives. *Geol. Soc. Am. Bull.* **112**, 324–350 (2000).
3. P. Patriat, J. Achache, India–Eurasia collision chronology has implications for crustal shortening and driving mechanism of plates. *Nature* **311**, 615–621 (1984).
4. T. H. Torsvik *et al*., Phanerozoic polar wander, palaeogeography and dynamics. *Earth Sci. Rev.* **114**, 325–368 (2012).
5. A. Patzelt, H. Li, J. Wang, E. Appel, Palaeomagnetism of Cretaceous to tertiary sediments from southern Tibet: Evidence for the extent of the northern margin of India prior to the collision with Eurasia. *Tectonophysics* **259**, 259–284 (1996).
6. D. J. Van Hinsbergen *et al*., Restoration of Cenozoic deformation in Asia and the size of Greater India. *Tectonics* **30**, TC5003 (2011).
7. J. C. Aitchison *et al*., Remnants of a Cretaceous intra-oceanic subduction system within the Yarlung–Zangbo suture (southern Tibet). *Earth Planet. Sci. Lett.* **183**, 231–244 (2000).
8. S. Zahirovic *et al*., Insights on the kinematics of the India-Eurasia collision from global geodynamic models. *Geochem. Geophys. Geosyst.* **13**, 4 (2012).
9. O. Jagoutz, L. Royden, A. F. Holt, T. W. Becker, Anomalously fast convergence of India and Eurasia caused by double subduction. *Nat. Geosci.* **8**, 475–478 (2015).
10. P. Bouilhol, O. Jagoutz, J. M. Hanchar, F. O. Dudas, Dating the India–Eurasia collision through arc magmatic records. *Earth Planet. Sci. Lett.* **366**, 163–175 (2013).
11. O. Jagoutz, F. A. Macdonald, L. Royden, Low-latitude arc-continent collision as a driver for global cooling. *Proc. Natl. Acad. Sci. U.S.A.* **113**, 4935–4940 (2016).
12. M. G. Petterson, B. F. Windley, RbSr dating of the Kohistan arc-batholith in the Trans-Himalaya of north Pakistan, and tectonic implications. *Earth Planet. Sci. Lett.* **74**, 45–57 (1985).
13. P. C. Lippert, D. J. Van Hinsbergen, G. Dupont-Nivet, *Early Cretaceous to Present Latitude of the Central Proto-Tibetan Plateau: A Paleomagnetic Synthesis with Implications for Cenozoic Tectonics, Paleogeography, and Climate of Asia* (Geological Society of America Special Papers, 2014), vol. 507, pp. 1–21.
14. D. J. van Hinsbergen *et al*., Reconstructing Greater India: Paleogeographic, kinematic, and geodynamic perspectives. *Tectonophysics* **760**, 69–94 (2019).
15. E. Garzanti, Comment on "When and where did India and Asia collide?" by Jonathan C. Aitchison, Jason R. Ali, and Aileen M. Davis. *J. Geophys. Res. Solid Earth* **113**, B04411 (2008).
16. X. Hu *et al*., The timing of India-Asia collision onset—Facts, theories, controversies. *Earth Sci. Rev.* **160**, 264–299 (2016).
17. L.-L. Zhang, C.-Z. Liu, F.-Y. Wu, W.-Q. Ji, J.-G. Wang, Zedong terrane revisited: An intra-oceanic arc within Neo-Tethys or a part of the Asian active continental margin? *J. Asian Earth Sci.* **80**, 34–55 (2014).
18. J. Westerweel *et al*., Burma Terrane part of the Trans-Tethyan Arc during collision with India according to palaeomagnetic data. *Nat. Geosci.* **12**, 863–868 (2019).
19. R. A. Beck, D. W. Burbank, W. J. Sercombe, A. M. Khan, R. D. Lawrence, Late Cretaceous ophiolite obduction and Paleocene India-Asia collision in the westernmost Himalaya. *Geodin. Acta* **9**, 114–144 (1996).
20. P. Tapponnier, M. Mattauer, F. Proust, C. Cassaigneau, Mesozoic ophiolites, sutures, and large-scale tectonic movements in Afghanistan. *Earth Planet. Sci. Lett.* **52**, 355–371 (1981).
21. R. K. Tahirkheli, Geology of Kohistan and adjoining Eurasian and Indo-Pakistan continents, Pakistan. *Geolog. Bull. Univ. Peshawar* **11**, 1–30 (1979).
22. M. N. Ahmad, M. Yoshida, Y. Fujiwara, Paleomagnetic study of Utror volcanic formation: Remagnetizations and postfolding rotations in Utror area, Kohistan arc, northern Pakistan. *Earth Planets Space* **52**, 425–436 (2000).
23. C. Klootwijk *et al*., The extent of Greater India, II. Palaeomagnetic data from the Ladakh intrusives at Kargil, northwestern Himalayas. *Earth Planet. Sci. Lett.* **44**, 47–64 (1979).
24. H. Zaman, M. Torii, Palaeomagnetic study of Cretaceous red beds from the eastern Hindukush ranges, northern Pakistan: Palaeoreconstruction of the Kohistan–Karakoram composite unit before the India–Asia collision. *Geophys. J. Int.* **136**, 719–738 (1999).
25. H. Zaman, Y.-i. Otofuji, S. R. Khan, M. N. Ahmad, New paleomagnetic results from the northern margin of the Kohistan Island Arc. *Arab. J. Geosci.* **6**, 1041–1054 (2013).
26. W. J. Dunlap, R. Wysoczanski, Thermal evidence for early Cretaceous metamorphism in the Shyok suture zone and age of the Khardung volcanic rocks, Ladakh, India. *J. Asian Earth Sci.* **20**, 481–490 (2002).
27. N. Lakhan *et al*., Zircon U–Pb geochronology, mineral and whole-rock geochemistry of the Khardung volcanics, Ladakh Himalaya, India: Implications for Late Cretaceous to Palaeogene continental arc magmatism. *Geol. J.* **55**, 3297–3320 (2020).
28. J. S. Barnet *et al*., A high-fidelity benthic stable isotope record of late Cretaceous–early Eocene climate change and carbon-cycling. *Paleoceanogr. Paleoclimatol.* **34**, 672–691 (2019).
29. R. Van der Voo, The reliability of paleomagnetic data. *Tectonophysics* **184**, 1–9 (1990).
30. G. Watson, A test for randomness of directions. *Geophys. J. Int.* **7**, 160–161 (1956).
31. K. L. Buchan, Key paleomagnetic poles and their use in proterozoic continent and supercontinent reconstructions: A review. *Precambrian Res.* **238**, 93–110 (2013).
32. M. H. Deenen, C. G. Langereis, D. J. van Hinsbergen, A. J. Biggin, Geomagnetic secular variation and the statistics of palaeomagnetic directions. *Geophys. J. Int.* **186**, 509–520 (2011).
33. S. C. Cande, P. Patriat, J. Dyment, Motion between the Indian, Antarctic and African plates in the early Cenozoic. *Geophys. J. Int.* **183**, 127–149 (2010).
34. Y. Najman *et al*., The Tethyan Himalayan detrital record shows that India–Asia terminal collision occurred by 54 Ma in the western Himalaya. *Earth Planet. Sci. Lett.* **459**, 301–310 (2017).
35. N. L. Borneman *et al*., Age and structure of the Shyok suture in the Ladakh region of northwestern India: Implications for slip on the Karakoram fault system. *Tectonics* **34**, 2011–2033 (2015).
36. R. Upadhyay, A. K. Sinha, R. Chandra, H. Rai, Tectonic and magmatic evolution of the eastern Karakoram, India. *Geodin. Acta* **12**, 341–358 (1999).
37. R. F. Weinberg, W. J. Dunlap, Growth and deformation of the Ladakh batholith, northwest Himalayas: Implications for timing of continental collision and origin of calc-alkaline batholiths. *J. Geol.* **108**, 303–320 (2000).
38. N. X. Thanh *et al*., A Cretaceous forearc ophiolite in the Shyok suture zone, Ladakh, NW India: Implications for the tectonic evolution of the northwest Himalaya. *Lithos* **155**, 81–93 (2012).
39. L. Guangwei *et al*., In-situ detrital zircon geochronology and Hf isotopic analyses from upper Triassic Tethys sequence strata. *Earth Planet. Sci. Lett.* **297**, 461–470 (2010).
40. F. Cai *et al*., Late Triassic paleogeographic reconstruction along the Neo–Tethyan ocean margins, southern Tibet. *Earth Planet. Sci. Lett.* **435**, 105–114 (2016).
41. M. Murphy *et al*., Southward propagation of the Karakoram fault system, southwest Tibet: Timing and magnitude of slip. *Geology* **28**, 451–454 (2000).
42. J. Burg, G. Chen, Tectonics and structural zonation of southern Tibet, China. *Nature* **311**, 219–223 (1984).

43. A. Yin *et al*., Tertiary deformation history of southeastern and southwestern Tibet during the Indo-Asian collision. *Geol. Soc. Am. Bull.* **111**, 1644–1664 (1999).
44. P. Kapp, P. G. DeCelles, Mesozoic–Cenozoic geological evolution of the Himalayan-Tibetan orogen and working tectonic hypotheses. *Am. J. Sci.* **319**, 159–254 (2019).
45. R. Hébert *et al*., The Indus–Yarlung Zangbo ophiolites from Nanga Parbat to Namche Barwa syntaxes, southern Tibet: First synthesis of petrology, geochemistry, and geochronology with incidences on geodynamic reconstructions of Neo-Tethys. *Gondwana Res.* **22**, 377–397 (2012).
46. X. M. Hu, J. G. Wang, M. BouDagher-Fadel, E. Garzanti, W. An, New insights into the timing of the India-Asia collision from the Paleogene Quxia and Jialazi formations of the Xigaze forearc basin, South Tibet. *Gondwana Res.* **32**, 76–92 (2016).
47. O. Jagoutz, P. Bouilhol, U. Schaltegger, O. Müntener, The isotopic evolution of the Kohistan Ladakh arc from subduction initiation to continent arc collision. *Geol. Soc. Lond. Spec. Publ.* **483**, 165–182 (2019).
48. P. DeCelles, P. Kapp, G. Gehrels, L. Ding, Paleocene-Eocene foreland basin evolution in the Himalaya of southern Tibet and Nepal: Implications for the age of initial India-Asia collision. *Tectonics* **33**, 824–849 (2014).
49. P. Molnar, J. M. Stock, Slowing of India's convergence with Eurasia since 20 Ma and its implications for Tibetan mantle dynamics. *Tectonics* **28**, TC3001 (2009).
50. P. H. Leloup *et al*., New constraints on the structure, thermochronology, and timing of the Ailao Shan-Red River shear zone, SE Asia. *J. Geophys. Res. Solid Earth* **106**, 6683–6732 (2001).
51. J.-P. Burg, P. Bouilhol, Timeline of the South Tibet–Himalayan belt: The geochronological record of subduction, collision, and underthrusting from zircon and monazite U–Pb ages. *Can. J. Earth Sci.* **56**, 1318–1332 (2019).
52. P. G. DeCelles, D. M. Robinson, G. Zandt, Implications of shortening in the Himalayan fold-thrust belt for uplift of the Tibetan Plateau. *Tectonics* **21**, 12-11–12-25 (2002).
53. C. Li, R. D. Van der Hilst, A. S. Meltzer, E. R. Engdahl, Subduction of the Indian lithosphere beneath the Tibetan Plateau and Burma. *Earth Planet. Sci. Lett.* **274**, 157–168 (2008).
54. J. M. Mattinson, Zircon U–Pb chemical abrasion ("CA-TIMS") method: Combined annealing and multi-step partial dissolution analysis for improved precision and accuracy of zircon ages. *Chem. Geol.* **220**, 47–66 (2005).
55. M. P. Eddy *et al*., High-resolution temporal and stratigraphic record of Siletzia's accretion and triple junction migration from nonmarine sedimentary basins in central and western Washington. *Bulletin* **128**, 425–441 (2016).
56. N. M. McLean, D. J. Condon, B. Schoene, S. A. Bowring, Evaluating uncertainties in the calibration of isotopic reference materials and multi-element isotopic tracers (EARTHTIME Tracer Calibration Part II). *Geochim. Cosmochim. Acta* **164**, 481–501 (2015).
57. H. K. Krogh, J. A. Maeland, O. Tönder, Indirect haemagglutination for demonstration of antibodies to stratum corneum of skin. *Int. Arch. Allergy Immunol.* **42**, 493–502 (1972).
58. A. O. Nier, A redetermination of the relative abundances of the isotopes of carbon, nitrogen, oxygen, argon, and potassium. *Phys. Rev.* **77**, 789–793 (1950).
59. J. Hiess, D. J. Condon, N. McLean, S. R. Noble, 238U/235U systematics in terrestrial uranium-bearing minerals. *Science* **335**, 1610–1614 (2012).
60. U. Schärer, The effect of initial230Th disequilibrium on young UPb ages: The Makalu case, Himalaya. *Earth Planet. Sci. Lett.* **67**, 191–204 (1984).
61. L. L. Claiborne *et al*., "Zircon as magma monitor: Robust, temperature-dependent partition coefficients from glass and zircon surface and rim measurements from natural systems" in *Microstructural Geochronology: Planetary Records Down to Atom Scale*, D. E. Moser, F. Corfu, J. R. Darling, S. M. Reddy, K. Tait, Eds. (American Geophysical Union, 2018), pp. 1–33.
62. J. F. Bowring, N. M. McLean, S. Bowring, Engineering cyber infrastructure for U-Pb geochronology: Tripoli and U-Pb_Redux. *Geochem. Geophys. Geosyst.*, 10.1029/2010GC003479 (2011).
63. N. M. McLean, J. F. Bowring, S. A. Bowring, An algorithm for U-Pb isotope dilution data reduction and uncertainty propagation. *Geochem. Geophys. Geosyst.*, 10.1029/2010GC003478 (2011).
64. A. H. Jaffey, K. F. Flynn, L. E. Glendenin, W. C. Bentley, A. M. Essling, Precision measurement of half-lives and specific activities of U 235 and U 238. *Phys. Rev. C* **4**, 1889–1906 (1971).
65. J. L. Kirschvink, R. E. Kopp, T. D. Raub, C. T. Baumgartner, J. W. Holt, Rapid, precise, and high-sensitivity acquisition of paleomagnetic and rock-magnetic data: Development of a low-noise automatic sample changing system for superconducting rock magnetometers. *Geochem. Geophys. Geosyst.*, 10.1029/2007GC001856 (2008).
66. J. Kirschvink, The least-squares line and plane and the analysis of palaeomagnetic data. *Geophys. J. Int.* **62**, 699–718 (1980).
67. R. A. Fisher, Dispersion on a sphere. *Proc. R. Soc. Lond. A Math. Phys. Sci.* **217**, 295–305 (1953).
68. N. I. Fisher, T. Lewis, Estimating the common mean direction of several circular or spherical distributions with differing dispersions. *Biometrika* **70**, 333–341 (1983).
69. L. Tauxe, *Essentials of Paleomagnetism* (University of California Press, 2010).
70. L. Tauxe *et al*., PmagPy: Software package for paleomagnetic data analysis and a bridge to the magnetics information consortium (MagIC) database. *Geochem. Geophys. Geosyst.* **17**, 2450–2463 (2016).
71. S. A. MacLennan *et al*., Geologic evidence for an icehouse Earth before the Sturtian global glaciation. *Sci. Adv.* **6**, eaay6647 (2020).